Accepted to ApJ: October 10, 2016
Preprint typeset using LaTeX style emulateapj v. 5/2/11

arXiv:1610.05310v1 [astro-ph.GA] 17 Oct 2016

STAR FORMATION IN INTERMEDIATE REDSHIFT $0.2 < Z < 0.7$ BRIGHTEST CLUSTER GALAXIES.

Kevin C. Cooke[1], Christopher P. O'Dea[1,2], Stefi A. Baum[1,2], Grant R. Tremblay[3], Isabella G. Cox[1], Michael D. Gladders[4]

[1]School of Physics and Astronomy, Rochester Institute of Technology, Rochester, NY 14623, USA
[2]Department of Physics and Astronomy, University of Manitoba, Winnipeg, MB R3T 2N2, Canada
[3]Department of Astronomy and Yale Center for Astronomy and Astrophysics, Yale University, 52 Hillhouse Ave., New Haven, CT 06511, USA
[4]Department of Astronomy and Astrophysics and Kavli Institute for Cosmological Physics, University of Chicago, 5640 South Ellis Avenue, Chicago, IL 60637, USA

Accepted to ApJ: *October 10, 2016*

ABSTRACT

We present a multi-wavelength photometric and spectroscopic study of 42 Brightest Cluster Galaxies (BCGs) in two samples of clusters of galaxies chosen for the study of gravitational lensing. The study's initial sample combines 25 BCGs from the Cluster Lensing and Supernova Survey with Hubble (CLASH) sample and 37 BCGs from the Sloan Giant Arcs Survey (SGAS) with a total redshift range of $0.2 < z < 0.7$ Using archival GALEX, HST, WISE, Herschel, and VLA data we determine the BCGs' stellar mass, radio power, and star formation rates. The radio power is higher than expected if due to star formation, consistent with the BCGs being AGN-powered radio sources. This suggests that the AGN and star formation are both fueled by cold gas in the host galaxy. The specific star formation rate (sSFR) is low and constant with redshift. The mean sSFR is 9.42×10^{-12} yr^{-1} which corresponds to a mass doubling time of 105 billion years. These findings are consistent with models for hierarchical formation of BCGs which suggest that star formation is no longer a significant channel for galaxy growth for z $\leq$ 1. Instead, stellar growth (of order a factor of at least 2) during this period is expected to occur mainly via minor dry mergers

Subject headings: galaxies: clusters, galaxies: elliptical and lenticular, cD, galaxies: clusters: intracluster medium, galaxies: star formation

1. INTRODUCTION

The most massive and luminous galaxies observed are the Brightest Cluster Galaxies. They are typically located in the centers of galaxy clusters, indicating a relaxed position in the cluster potential. Their formation models are environmentally dependent, and distinct from typical elliptical galaxies (e.g., Lin & Mohr 2004; Brough et al. 2005; De Lucia & Blaizot 2007). BCGs are also more likely to host active galactic nuclei (AGNs) than other galaxies of the same stellar mass (e.g., Best et al. 2007; Von Der Linden et al. 2007). This indicates that these objects play a pivotal role in quenching cooling flows and star formation in clusters (McNamara & Nulsen 2007, 2012; Fabian 2012). BCGs have been recently shown to lie off the standard scaling relations of early-type galaxies (e.g., Lauer et al. 2007; Von Der Linden et al. 2007; Bernardi et al. 2007; Bernardi 2009). In particular, they show excess luminosity (or stellar mass) above the prediction of the standard Faber-Jackson relation at high galaxy masses (e.g., Lauer et al. 2014).

Stellar population synthesis models suggest that the bulk of star formation in most massive galaxies took place prior to $z \sim 2$ (e.g., Thomas et al. 2005; Treu et al. 2005; Jimenez et al. 2007). Semi-analytical models also suggest that the stars that make up most of the BCG mass are formed very early on (80% by $z \sim 3$; De Lucia et al. (2006); De Lucia & Blaizot (2007)). Only after most stars have been formed does the final galaxy assembly take place via merging. The final galaxy mergers in BCG formation ($z < 1$) are expected to be predominantly dissipationless (or dry, i.e., not involving large amounts of gas; Khochfar & Burkert (2003); De Lucia & Blaizot (2007); Vulcani et al. (2016)).

Thus, a strong prediction of the hierarchical galaxy formation models is that at $z < 1$, star formation should make a only minor contribution to the growth of the stellar mass of BCGs. This has been confirmed at low redshift (e.g., Pipino et al. 2009; Donahue et al. 2010; Wang et al. 2010; Liu et al. 2012; Fraser-McKelvie et al. 2014). The vast majority of the BCGs studied previously have been at $z < 0.3$. McDonald et al. (2016) explored a much larger redshift range from $0.25 < z < 1.25$ and found that BCG star formation transitions from a disturbed cluster paradigm at $z > 0.6$ to a cool-core paradigm at $z = 0$. They also find that at $z \sim 0.4$, 20% of BCGs are forming stars at > 10 M$_\odot$/yr. To investigate this transition era, we present a study of star formation in two samples of BCGs (in clusters chosen for the study of gravitational lensing) which lie in the range $0.2 < z < 0.7$.

The outline for the paper is as follows. In Section 2, we discuss the sample selection criteria. In Section 3, we discuss the archival data used in the analysis. In Section 4, we discuss how we estimated the star formation rates, stellar masses, and radio power for the BCGs. In Section 5, we discuss the implications for formation models of BCGs. In Section 6, we give our conclusions.

This paper uses the current Lambda/Cold Dark Matter (ΛCDM) parameters of $H_0 = 70$ Mpc^{-1} km s^{-1}, $\Omega_M = 0.3$, and $\Omega_{vac} = 0.7$.

2. SAMPLE SELECTION

kcc7952@rit.edu

We studied all the BCGs from two samples of clusters selected for studies of gravitational lensing - the Sloan Giant Arcs Survey (SGAS) (Bayliss et al. 2011) and the Cluster Lensing and Supernova Survey with Hubble (CLASH) (Postman et al. 2012). The two samples cover a redshift range $0.2 < z < 0.7$. The clusters were not chosen on the basis of the star formation properties of the BCGs. The coordinates, redshifts, and modeled stellar mass of this BCG sample are described in Table 1 and their star formation rates from UV and Optical methods are listed in Table 2.

The 37 clusters in SGAS includes clusters selected from two different surveys and methods (Oguri et al. 2012). The first method is visual inspection of SDSS photometry of BCGs for strongly lensing systems (Bayliss et al. (2011), M. D. Gladders et al., in preparation). The second method is a "blind study" in which SDSS g-band images of the 240 most massive clusters in the SDSS are selected based on lensing strength (Hennawi et al. 2008).

The selection criteria for the 25 CLASH clusters is discussed in detail by Postman et al. (2012). They selected 20 massive clusters from X-ray-based compilations of dynamically relaxed systems. Sixteen of these 20 clusters were taken from the Allen et al. (2008) compilation of massive relaxed clusters. An additional five clusters were added due to their exceptional strength as gravitational lenses (Einstein radii > 35"). The star formation properties of the CLASH BCGs are discussed independently (Fogarty et al. 2015; Donahue et al. 2015) with results which are in agreement with those reported here.

3. ARCHIVAL DATA

3.1. *Galaxy Evolution Explorer Observations*

In order to measure the population of young, massive stars in BCGs we obtained archival far-UV (FUV) and near-UV (NUV) band total pipeline photometric magnitudes from the GR6/GR7 release of the Galaxy Evolution Explorer (GALEX) (Martin et al. 2005). GALEX photometry is taken using a 50 cm diameter Richey-Chretien telescope with a 1.2 degree circular field of view. To correct for galactic extinction, E(B-V) values are retrieved from the GALEXview webpage for each of the target locations observed by GALEX (Morrissey et al. 2007). Internal extinction is not corrected for due to Hα being redshifted out of SDSS spectral coverage for much of our sample. This prevents the use of the Balmer decrement to approximate internal dust levels across our entire sample. Our sample K-corrections are not calculated in the UV due to the presence of limits in the SDSS observations necessary for k-correction calculation. Previous CLASH UV findings (Donahue et al. 2015) have found k-corrections are less than 10% and do not significantly effect results. Archival data is a mixture of All Sky and Medium Imaging with depths of 20.5 and 23.5 m_{AB} respectively. For the farthest and least sensitive AIS case, MACS1149.6+2223, this corresponds to a SFR upper limit of 4.84 $M_\odot$/yr. Even in the worst case scenario, this is still sensitive enough to detect examples of exceptionally high star formation and we only use these limits in cases with no optical emission line detections.

The UV contribution from an old stellar population, called the "UV-upturn" (O'Connell 1999), can be addressed through modeling of the spectra of other ellipticals in the BCG's cluster (e.g. Hicks et al. 2010; Fogarty et al. 2015). In order to predict the old stellar UV contribution in a given target, we acquired a UV-Optical-NIR spectrum previously constructed using satellite ellipticals in the CLASH sample clusters (Fogarty et al. 2015, and private communication). These templates are composites of quiescent populations and do not include ongoing star formation components. To approximate the UV from old stars, Fogarty et al. (2015) scaled their template to the available UV-Optical-NIR observations of the CLASH BCGs and derived a modeled J-band flux. The correlation between J-band and NUV for old stellar populations in BCGs prescribed in Table 5 of Hicks et al. (2010) was then used to generate an old stellar NUV flux. We performed our SED scaling using the I-band from SDSS. Z-band was not used due to the more common occurrence of upper limits.

3.2. *Sloan Digital Sky Survey Observations*

In order to measure the optical SED of the BCGs, we use the Catalog Archive Server Jobs System (CASJOBS) (Li & Thakar 2008) to obtain archival *ugriz* Petrosian magnitudes (Petrosian 1976) from the Sloan Digital Sky Survey (SDSS) (Gunn et al. 2006). SDSS reports that the pipeline Petrosian magnitudes reliably include 80% of a galaxy's light independent of distance (Blanton et al. 2001). We use Data Release 12 (DR12) results (Alam et al. 2015). If the observed Petrosian magnitudes are lower than SDSS *ugriz* limiting magnitudes [22.0, 22.2, 22.2, 21.3, 20.5] respectively, the galaxy is considered a non-detection and the Petrosian magnitude is used as a limit (Ahn et al. 2012). We take extinction magnitudes from the photoObj SDSS tables to correct Milky Way foreground extinction. Foreground extinction magnitudes assume a Milky Way Galaxy extinction map from (Schlafly & Finkbeiner 2011) assuming a galactic reddening of $R_v = 3.1$.

To measure the emission line features of the BCGs, we use archival spectral measurements and errors from SDSS DR12. SDSS multi-object spectroscopy is taken using fibers that subtend 3" on the sky, large enough to include the majority of a given BCG. The effects of this fixed aperture size, and its relation to the other apertures used for the photometry, is discussed in Section 4. Emission and absorption features in SDSS spectra are fit and stored in the galspecLine view in the publicly available Sky Server database of SDSS as a feature of the standard pipeline reduction of DR12. Foreground extinction was corrected for using the Milky Way extinctions calculated above.

3.3. *Wide-Field Infrared Survey Explorer Observations*

The Wide-Field Infrared Survey Explorer (WISE) is a NASA space telescope (Wright et al. 2010) designed to perform an all sky survey using four bands. To constrain the old stellar population during SED fitting, we retrieved WISE profile fit 3.4, 4.6, 11 and 22 μm (W1, W2, W3, W4) magnitudes from the NASA/IPAC Infrared Science Archive (IRSA) AllWISE Source Catalog (Cutri & et al. 2013). The AllWISE catalog co-added exposures from the cryogenic and NEOWISE phases resulting in 5σ flux detections at 16.9, 16.0, 11.5 and 8.0 m_{Vega} for W1, W2, W3 and W4 respectively. Magnitudes reported are reported with photometric quality flags. We

treat data with flag U (95% confidence upper limit) and C ($2 < SNR < 3$) as upper limits, and trust the stronger A ($SNR > 10$) and B ($3< SNR < 10$) flags as detections. Extinction in the infrared is negligible and is not corrected for in our work.

3.4. *Herschel Space Observatory Observations*

To better characterize absorbed and re-emitted starlight from dust, we obtained archival data from the Herschel Space Observatory (HSO) - a European Space Agency (ESA) built far infrared/sub-mm telescope launched in 2009 (Pilbratt et al. 2010). Archival Photoconductor Array Camera and Spectrometer (PACS) green band (100 μm), and red band (160 μm) photometry were acquired through the Herschel Science Archive. A subset of CLASH galaxies were observed by the Herschel Lensing Survey (Egami et al. 2010) with flux limit of 2.4 mJy (100 μm) and 4.7 mJy (160 μm). 1 SGAS target was observed by Malhotra (2011); SDSSJ0915+3826 to limits of 5.2 mJy (100 μm) and 9.9 mJy (160 μm). Another was observed by Lutz (2010); SDSSJ1343+4155 to limits of 4.42 mJy (70 μm) 9.9 mJy (160 μm).

To guarantee up-to-date calibrations for our faint sources, we re-reduced this sample's Herschel PACS photometry with Herschel Interactive Programming Environment (HIPE) from the raw level 1 maps to the science quality level 2.5 using the MadMap pipeline (Cantalupo et al. 2010). This step is done in order to examine images with the latest Herschel PACS calibration files. Level 1 maps was retrieved from the Herschel Science Archive (HSA) with PACS calibration version PACS_CAL_69_0. MadMap removes the most common noise source in Herschel PACS images, the 1/f noise. 1/f noise is the randomized photon noise over time the detector observes along with the target photons. Once the level 2.5 maps are produced from HIPE's reduction process, the task `sourceExtractor` was used to measure individual object fluxes and errors while correcting for sky background. Afterward, we ran the `sourceExtractor` task built into HIPE to detect objects with a SNR threshold of 3 using a gaussian with band-specific FWHMs of 10.5", 6.67", and 5.4" for red (160 μm), green (100 μm), and blue (70 μm) channels respectively (PACS Handbook).

3.5. *Very Large Array Observations*

In order to quantify the activity of the supermassive black hole in each BCG, Karl G. Jansky Very Large Array (VLA) (Thompson et al. 1980) radio observations of observer-frame 1.4 GHz flux are taken from the 2014 version of the NRAO VLA Sky Survey (NVSS) (Condon et al. 1998) and the Faint Images of the Radio Sky at Twenty-Centimeters (FIRST) Survey Catalog (Helfand et al. 2015). NVSS is designed to observe 1.4 GHz emission at a low resolution of 45" across the entire sky north of δ = -40°. FIRST is a large-scale (>10,000 deg^2) survey which observed the radio sky at a resolution of 5" from 1993 to 2011 (Helfand et al. 2015).

For objects with observations in both the NVSS and FIRST archival catalogs, preference is given to FIRST observations which have a better angular resolution as well as an rms of 0.15 mJy versus NVSS's rms of 0.45 mJy per beam. Nine BCGs observed by NVSS and FIRST do not have fully reduced photometry available in the published catalogs. We used the Common Astronomy Software Applications (CASA) (McMullin et al. 2007) package to perform background subtraction and record the target radio flux or the upper limit if there is no visible source in the image. Observations were k-corrected and extrapolated to target-frame 1.4 GHz using a spectral index of 0.75, common for BCGs (Hlavacek-Larrondo et al. 2013; Giacintucci et al. 2014).

4. ANALYSIS

BCG luminosity and stellar mass estimates were derived from the publicly available galaxy SED fitting software MAGPHYS (da Cunha et al. 2008). MAGPHYS fits the SED of each galaxy using two components; UV to optical & near to far infrared. The fitting is done self-consistently, modeling the FIR flux considering the star formation fitted to the UV and optical. Rather than the default Bruzual (2007) models, we use the Bruzual & Charlot (2003) stellar population models found to successfully model BCGs in the past (e.g. Lidman et al. 2012). The infrared models include PAH, cold (15-25 K) , warm (30-60 K), and hot (130-250 K) dust components. MAGPHYS fitted values used here include the total stellar mass. Flux reduction due to cosmological expansion is accounted for by MAGPHYS before the fitting process using redshifts reported by Postman et al. (2012) for CLASH targets and Alam et al. (2015) for SDSS targets.

5 of the SGAS sample BCGs lacked SDSS photometric or spectroscopic redshifts at the time of this work and could not be accurately modeled: SDSSJ0333-0651, SDSSJ1420+3955, SDSSJ1522+2535, SDSSJ1621+0607, and SDSSJ2243-0935. Additionally, SDSSJ0915+3826 and SDSSJ0928+2031 both had failed fits with infinite χ^2. This is believed to have occurred due to a combination of lack of NIR data as well as having the majority of its SDSS fluxes as limits. These two are removed from the following statistics and plots. An additional 13 targets had no SDSS spectra or GALEX photometry within 10", resulting in the final sample of 42 BCGs.

Total star formation rate estimates from MAGPHYS are not used due to the poor infrared coverage of the SGAS sample. The fitting procedure systematically overestimates the far infrared luminosity in the SGAS sample due to lack of constraints. This high estimated infrared luminosity corresponds to total star formation rates much higher than that what is consistent with the lack of dust and substructure seen in HST photometry. However, the stellar mass estimates from MAGPHYS use the well characterized optical-NIR continuum and are used further in this study. For this study's results, we use the Kennicutt (1998) calibrations for optical emission line SFR estimates. We use SDSS Hα fluxes where possible, followed by [OII] when Hα was redshifted out of the SDSS coverage. GALEX NUV photometry was retrieved in the case where SDSS spectra are not available and we approximate the SFR using the Kennicutt (1998) UV continuum calibration.

The SGAS subsample SFRs are predominantly approximated using Hα and [OII] emission measured through the 3" diameter fibers of the SDSS multi object spectrograph. CLASH targets not observed by SDSS have SFRs approximated through GALEX NUV flux measured through elliptical Kron apertures in which the ra-

dius is 2.5 times the first moment of the target's radial profile. The Kron radii used for targets in our sample range from 3-5" in radius. CLASH SFRs are likely to be more accurate than SDSS fibers, which may miss star forming knots in a given galaxy. One recent example is Tremblay et al. (e.g. 2014)'s study of star formation filaments in a merging system of two massive ellipticals. Slit spectroscopy using the ALFOSC spectrograph on the Nordic Optical Telescope found 1.7 times the SDSS Hα flux reported in SDSS Data Release 9. To correct for this effect would require a priori knowledge of the distribution, shape, and intensity of star forming knots in all galaxies in our sample, so we leave the SDSS fluxes as reported by the pipeline. Thus, the SGAS SFRs estimated using SDSS spectra will likely be lower limits to the true SFR.

Additionally, as a sanity check for our MAGPHYS stellar mass results, we compare with previous estimates of the CLASH subsample from Burke et al. (2015) and we are within 30%. For example, RX J1532+30's stellar mass is estimated by Burke et al. (2015) to be $2.20 \pm 0.05 \times 10^{11}$ $M_\odot$ while we estimate $2.88 \pm 0.06 \times 10^{11}$ $M_\odot$. Their methodology uses magnitudes from the Postman et al. (2012) observations fit to a spectral energy distribution produced by Bruzual & Charlot (2003)'s solar metallicity models. The combined CLASH-SGAS sample has a mean stellar mass of 7.52×10^{11} $M_\odot$ and standard deviation of 6.22×10^{11} $M_\odot$.

5. DISCUSSION

5.1. *Dependencies With Mass*

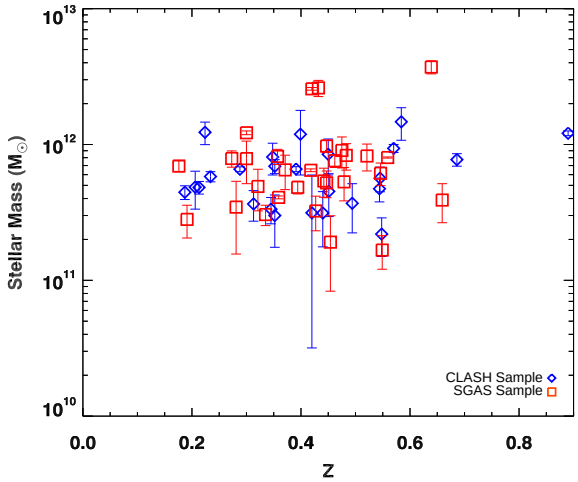

Figure 1. BCG stellar mass versus redshift of both samples as fit by MAGPHYS. Red squares are SGAS sample galaxies. Blue diamonds are CLASH sample galaxies. Error bars are 1σ.

In Figure 1 we show the total stellar masses (estimated as described in § 4) as a function of redshift. There is no trend of stellar mass with redshift over the range z = 0.2 - 0.7. We confirmed that the masses of the CLASH and SGAS samples are statistically similar using a Kolmogorov-Smirnov test implemented using IDL's `kstwo` procedure on both samples. The probability the subsamples are identical is 0.75, with a maximum difference of 1.5% between subsample distribution functions as seen in Figure 2.

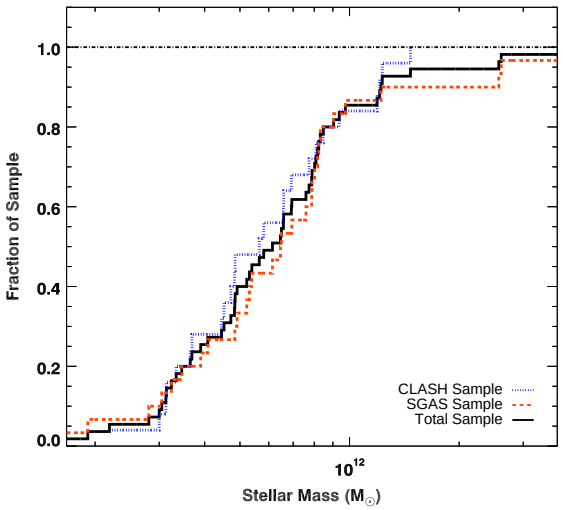

Figure 2. Cumulative histogram of stellar masses calculated for CLASH (dotted blue line), SGAS (bashed red line), and the combined sample (solid black line).

In Figure 3 we examine the importance of star formation activity to a galaxy's evolution by comparing the star formation rate with the total stellar mass. Previous results show that at redshifts $0 < z < 2$, star forming galaxies in general show a correlation between stellar mass and star formation rate which has been called a Star Formation Main Sequence (SFMS) (e.g. Brinchmann et al. 2004; Noeske et al. 2007; Elbaz et al. 2007; Daddi et al. 2007; Santini et al. 2009; Lara-López et al. 2010; Zahid et al. 2013; Vaddi et al. 2016). No SFMS trend is seen in our sample. This corroborates previous results by Lee et al. (e.g. 2015) in which the SFMS is nearly flat (or absent) above 10^{11} $M_\odot$.

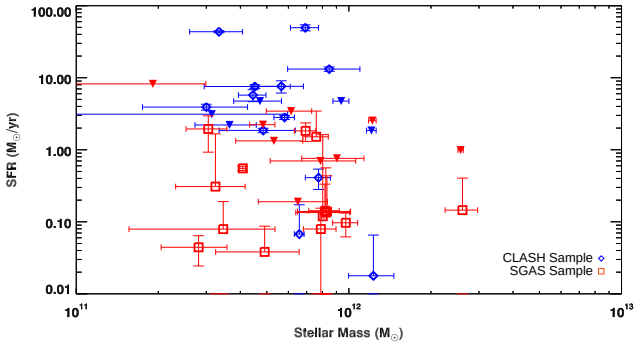

Figure 3. Star formation rate versus stellar mass of both samples as fit by MAGPHYS. Red squares are SGAS sample galaxies. Blue diamonds are CLASH sample galaxies. Error bars are 1σ. Down facing triangles are upper limits. Missing lower limit bars are an artifact of plotting large errors on a log scale.

5.2. *Radio Behavior*

The observed radio powers and upper limits of the BCGs (Figure 4) are 1-2 orders of magnitude above the radio powers expected if due solely to star formation esti-

mated following Condon (1992). This suggests that the radio emission is being powered by the AGN in these BCGs. This is consistent with previous evidence that BCGs are often radio loud. The fraction of galaxies which are radio loud increases with galaxy mass (e.g., Auriemma et al. 1977; Dressel 1981; Ledlow & Owen 1996; Best et al. 2005; Von Der Linden et al. 2007). In addition, the average (and maximum) observed radio power increases with galaxy mass (e.g., Brown et al. 2011; Vaddi et al. 2016). This suggests that the source of fuel for AGN activity increases with galaxy mass; though radio power and mechanical power are not just a simple function of the accretion rate (e.g., McNamara & Nulsen 2007, 2012; Best & Heckman 2012). Nevertheless, this is consistent with cold gas being the source of fuel for both the AGN and star formation activity. Cold gas has been suggested as the fuel for AGN activity (e.g., Pizzolato & Soker 2005; Gaspari et al. 2013, 2015; Li & Bryan 2014). There is evidence for infalling molecular gas in some BCGs, such as in A2597 (Tremblay et al. 2016).

BCGs are more often found to be radio loud than non-BCG galaxies of the same mass (Best et al. 2007; Von Der Linden et al. 2007). This suggests that the BCGs have an additional source of gas which is not present in non-BCG galaxies of the same mass. Alternately, BCGs could have larger mass black holes than non-BCG galaxies of the same stellar mass (e.g., Hlavacek-Larrondo et al. 2012). The additional source of gas in the BCGs is likely to be cooling from the hot ICM in cool-core clusters (e.g., Fabian 1994; Best et al. 2007; Sun 2009). The additional source of gas in the cool-core BCGs results in higher star formation than in the non-cool-core BCGs (see §5.3).

We find the range of BCG radio powers ($L_{1.4GHz} \approx 10^{24-25}$ W Hz^{-1}) lie in the FR II (Fanaroff & Riley 1974; Bridle 1984) regime. These radio powers are sufficient to provide significant mechanical mode feedback to the environment, quenching star formation in the BCG (McNamara & Nulsen 2007, 2012; Fabian 2012). A radio power of 10^{25} W Hz^{-1} corresponds to a νP_ν Luminosity of 10^{34} W. Assuming a 1% efficiency of conversion of jet power to radio power (Eilek & Shore 1989; Cavagnolo et al. 2010; Daly et al. 2012) and 10% conversion of rest mass energy to jet power gives a mass accretion rate of $\sim 10^{-4}$ M$_\odot$ yr^{-1} which is small compared to the SFR.

5.3. *Dependencies With Redshift*

We plot star formation rates vs redshift in Figure 5. The estimated star formation rates show no trend with redshift over the range z = 0.2 - 0.6. The SFR rates vary mostly between about 0.1 and 10 M$_\odot$ yr^{-1}. Examples of BCGs with high star formation rates are discussed in the Appendix and in Fogarty et al. (2015).

We show the specific star formation rate (sSFR, star formation rate per unit stellar mass, e.g., Brinchmann et al. 2004) in Figure 6. There is no trend in specific star formation rate with redshift over the range z=0.2 - 0.6. There is slight difference in the specific star formation rates of the SGAS and CLASH samples. For the combined MAGPHYS modeled dataset of 17 CLASH BCGs and 24 SGAS BCGs, IDL's `twosampt` task found that CLASH and SGAS have a probability of 49% of being the same distribution. This difference is likely due to the much smaller apertures used for measuring the Hα flux

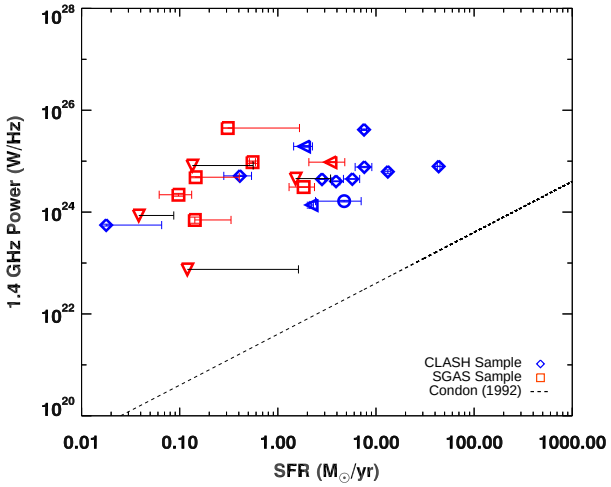

Figure 4. FIRST and NVSS 1.4 GHz rest frame emission assuming α=0.75. The representative radio emission due to a star formation dominated scenario is plotted with the dashed line (Condon 1992). Upper limits are the Downward facing triangles and from CASA-derived background corrected photometry on target locations. Red squares are SGAS sample galaxies. Blue diamonds are CLASH sample galaxies.Error bars are 1σ. Down facing and left facing triangles are upper limits for radio power and SFR respectively. Open circles indicate both quantities are upper limits. Missing lower limit bars are an artifact of plotting large errors on a log scale.

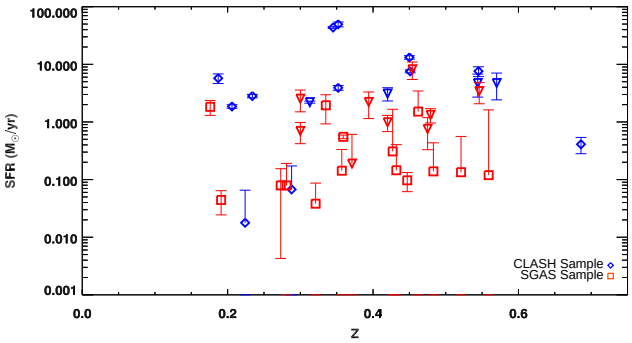

Figure 5. Star formation rate versus redshift of both samples. Red squares are SGAS sample galaxies. Blue diamonds are CLASH sample galaxies.Error bars are 1σ. Down facing triangles are upper limits. Missing lower limit bars are an artifact of plotting large errors on a log scale.

used in the SFR determinations of the SGAS sample.

The mean sSFR is 9.42 $\times$ 10^{-12} yr^{-1} in our study which corresponds to a mass doubling time of 105 billion years. Thus, the low SFR and sSFR suggest that galaxy growth via star formation in BCGs is minimal by $z \sim 0.7$ consistent with other studies of star formation in lower redshift BCGs (e.g. Pipino et al. 2009; Donahue et al. 2010; Wang et al. 2010; Liu et al. 2012; Fraser-McKelvie et al. 2014) as shown in Figure 7. The outlier BCGs which have higher than average star formation tend to be in cool-core clusters (e.g. Crawford et al. 1999; Edwards et al. 2007; O'Dea et al. 2008; O'Dea et al. 2010; Pipino et al. 2009; Hicks et al. 2010; Donahue et al. 2010; Wang et al. 2010; Pipino et al. 2011; Liu et al. 2012; Mittal et al. 2015; Tremblay et al. 2015; Donahue et al. 2015; Fogarty et al. 2015).

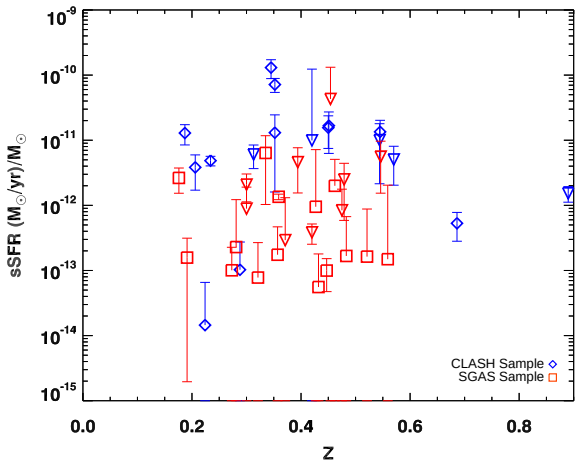

Figure 6. Specific star formation rate (sSFR) versus redshift of both samples. Red squares are SGAS sample galaxies. Blue diamonds are CLASH sample galaxies.Error bars are 1σ. Down facing triangles are upper limits. Missing lower limit bars are an artifact of plotting large errors on a log scale.

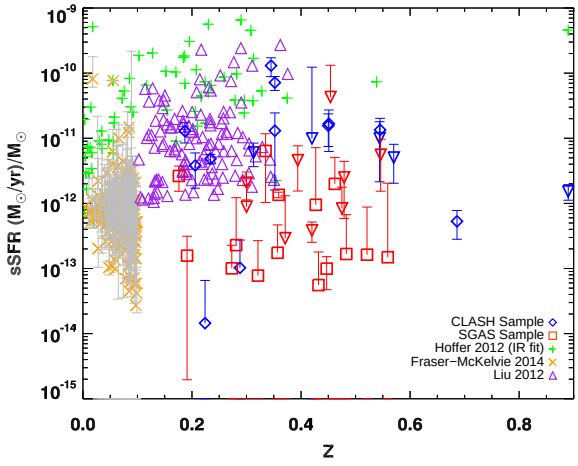

Figure 7. Specific star formation rate (sSFR) versus redshift which includes published values for lower redshift samples. Red squares are SGAS sample galaxies. Blue diamonds are CLASH sample galaxies.Error bars are 1σ. Down facing triangles are upper limits. Missing lower limit bars are an artifact of plotting large errors on a log scale.

5.4. *Growth by Mergers?*

Growth of the mass of BCGs by mechanisms which do not involve star formation (e.g., dry mergers) is not ruled out by this study of star formation. However, the lack of a redshift dependence to the BCG stellar mass (Figure 1) rules out a *large* gain in stellar mass over the redshift range $z = 0.3 - 0.6$ but probably allows a factor of two change in stellar mass over the redshift range $0 < z < 1$. The previous observational work is somewhat inconsistent. Figure 8 shows no clear trends in stellar mass with redshift, but the different samples have identified BCGs with different mass ranges. Whiley et al. (2008) find no evidence for factor of 2 growth in BCG mass since $z \sim 1$. Collins et al. (2009) find no difference in mass between BCGs at $z \sim 1.3$ and $z \sim 0$. Stott et al. (2011) show that BCGs have evolved little in size since $z \sim 1$. Inagaki et al. (2015) find no evidence for more than a few percent mass growth between $z \sim 0.4$ and $z \sim 0.2$. In contrast, other work has found evidence for the expected increase in BCG stellar mass by about a factor of 2 between $z \sim 1$ and $z \sim 0$ (e.g., Lidman et al. 2012; Lin et al. 2013; Burke & Collins 2013; Ascaso et al. 2014; Shankar et al. 2015). Our specific star formation rate results (Figure 7) corroborate McDonald et al. (2016)'s results, which BCGs are evolving slower than other galaxies in cluster environments. This would point to an alternate fuel source to keep BCGs mildly active when their satellites have been quenched. The differences between the conclusions of these studies may be due to how the samples were defined and the effects of progenitor bias (e.g., van Dokkum & Franx 1996; Hopkins et al. 2009; Saglia et al. 2010; Carollo et al. 2013; Shankar et al. 2015).

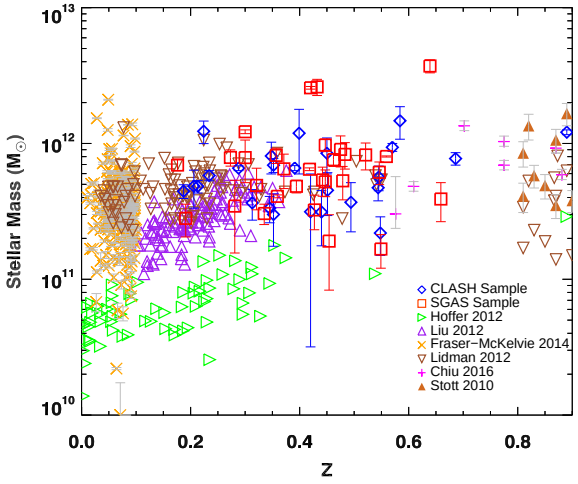

Figure 8. BCG stellar mass vs. redshift from different published samples of BCGs. Red squares are SGAS sample galaxies. Blue diamonds are CLASH sample galaxies. Error bars are 1σ. Down facing triangles are upper limits. Missing lower limit bars are an artifact of plotting large errors on a log scale.

For the subset of star-forming BCGs of the CLASH subsample, the fuel for the star formation is attributed to gas condensing out of a cool core (Fogarty et al. 2015; Donahue et al. 2015) which is consistent with the clusters having been X-ray selected. In the SGAS BCGs, X-ray evidence for cool cores is not yet available. We tentatively attribute the source of the fuel for star formation to a major merger in SDSSJ1336-0331 (Figure 9) and SDSSJ1531-3414 (Tremblay et al. 2014).

6. CONCLUSIONS

We present multi-wavelength estimates of star formation rates, and estimates of radio power and stellar mass for BCGs in two samples of clusters chosen for the study of gravitational lensing - CLASH and SGAS. The redshift range of the BCGs $0.2 < z < 0.7$ spans a large fraction of the range over which models of hierarchical galaxy formation suggest that star formation is no longer a significant channel for galaxy growth. Instead, stellar growth (of order a factor of at least 2) during this period

is expected to occur mainly via minor dry mergers (e.g., De Lucia & Blaizot 2007).

We find that SFRs and sSFRs are indeed low in BCGs $0.2 < z < 0.7$ (excluding some BCGs in cool-core clusters) consistent with results from samples of lower redshift BCGs (e.g., Pipino et al. 2009; Donahue et al. 2010; Wang et al. 2010; Liu et al. 2012; Fraser-McKelvie et al. 2014). The mean sSFR is 9.42×10^{-12} yr^{-1} which corresponds to a mass doubling time of 105 billion years. This is in agreement with the results of the numerical and semi-analytical work (e.g., Bell et al. 2006; De Lucia & Blaizot 2007) that galaxy growth by star formation is not significant at $z < 1$ in BCGs.

Based on their high radio power, the BCGs are AGN-powered radio sources, consistent with expectations for BCGs (Best et al. 2007; Von Der Linden et al. 2007). This is consistent with the AGN and star formation in these sources both being fueled by cold gas in the host galaxy.

We would like to thank the referee for constructive comments which helped make this paper a more robust study. We thank Kevin Fogarty of Johns Hopkins University for his advice on the nature of old stars in the UV and his UV model of SFR-poor elliptical satellites. We thank Elisabete Da Cunha for her upper-limit capable MAGPHYS code as well as her advice in its implementation. GRT acknowledges support from the NASA through Einstein Postdoctoral Fellowship Award Number PF-150128, issued by the Chandra X-ray Observatory Center, which is operated by the Smithsonian Astrophysical Observatory for and on behalf of NASA under contract NAS8-03060. Funding for SDSS-III has been provided by the Alfred P. Sloan Foundation, the Participating Institutions, the National Science Foundation, and the U.S. Department of Energy Office of Science. The SDSS-III web site is http://www.sdss3.org/. SDSS-III is managed by the Astrophysical Research Consortium for the Participating Institutions of the SDSS-III Collaboration including the University of Arizona, the Brazilian Participation Group, Brookhaven National Laboratory, Carnegie Mellon University, University of Florida, the French Participation Group, the German Participation Group, Harvard University, the Instituto de Astrofisica de Canarias, the Michigan State/Notre Dame/JINA Participation Group, Johns Hopkins University, Lawrence Berkeley National Laboratory, Max Planck Institute for Astrophysics, Max Planck Institute for Extraterrestrial Physics, New Mexico State University, New York University, Ohio State University, Pennsylvania State University, University of Portsmouth, Princeton University, the Spanish Participation Group, University of Tokyo, University of Utah, Vanderbilt University, University of Virginia, University of Washington, and Yale University. Based on observations made with the NASA Galaxy Evolution Explorer. GALEX is operated for NASA by the California Institute of Technology under NASA contract NAS5-98034. Based on observations made with the NASA/ESA Hubble Space Telescope, obtained from the Data Archive at the Space Telescope Science Institute, which is operated by the Association of Universities for Research in Astronomy, Inc., under NASA contract NAS 5-26555. These observations are associated with program #13003. This publication makes use of data products from the Wide-field Infrared Survey Explorer, which is a joint project of the University of California, Los Angeles, and the Jet Propulsion Laboratory/California Institute of Technology, funded by the National Aeronautics and Space Administration. Herschel is an ESA space observatory with science instruments provided by European-led Principal Investigator consortia and with important participation from NASA. HCSS / HSpot / HIPE is a joint development (are joint developments) by the Herschel Science Ground Segment Consortium, consisting of ESA, the NASA Herschel Science Center, and the HIFI, PACS and SPIRE consortia. The National Radio Astronomy Observatory is a facility of the National Science Foundation operated under cooperative agreement by Associated Universities, Inc.

REFERENCES

Ahn, C. P., Alexandroff, R., Allende Prieto, C., et al. 2012, ApJS, 203, 21
Alam, S., Albareti, F. D., Allende Prieto, C., et al. 2015, ApJS, 219, 12
Allen, S. W., Rapetti, D. A., Schmidt, R. W., et al. 2008, MNRAS, 383, 879
Ascaso, B., Lemaux, B. C., Lubin, L. M., et al. 2014, MNRAS, 442, 589
Auriemma, C., Perola, G. C., Ekers, R. D., et al. 1977, A&A, 57, 41
Bayliss, M. B., Hennawi, J. F., Gladders, M. D., et al. 2011, ApJS, 193, 27
Bell, E. F., Naab, T., McIntosh, D. H., et al. 2006, ApJ, 640, 241
Bernardi, M. 2009, MNRAS, 395, 1491
Bernardi, M., Hyde, J. B., Sheth, R. K., Miller, C. J., & Nichol, R. C. 2007, AJ, 133, 1741
Best, P. N., & Heckman, T. M. 2012, MNRAS, 421, 1569
Best, P. N., Kauffmann, G., Heckman, T. M., et al. 2005, MNRAS, 362, 25
Best, P. N., von der Linden, A., Kauffmann, G., Heckman, T. M., & Kaiser, C. R. 2007, MNRAS, 379, 894
Blanton, M. R., Dalcanton, J., Eisenstein, D., et al. 2001, AJ, 121, 2358
Bridle, A. H. 1984, AJ, 89, 979
Brinchmann, J., Charlot, S., White, S. D. M., et al. 2004, MNRAS, 351, 1151
Brough, S., Collins, C. A., Burke, D. J., Lynam, P. D., & Mann, R. G. 2005, MNRAS, 364, 1354
Brown, M. J. I., Jannuzi, B. T., Floyd, D. J. E., & Mould, J. R. 2011, ApJ, 731, L41
Bruzual, G. 2007, in Astronomical Society of the Pacific Conference Series, Vol. 374, From Stars to Galaxies: Building the Pieces to Build Up the Universe, ed. A. Vallenari, R. Tantalo, L. Portinari, & A. Moretti, 303
Bruzual, G., & Charlot, S. 2003, MNRAS, 344, 1000
Burke, C., & Collins, C. A. 2013, MNRAS, 434, 2856
Burke, C., Hilton, M., & Collins, C. 2015, MNRAS, arXiv:1503.04321v1
Cantalupo, C. M., Borrill, J. D., Jaffe, A. H., Kisner, T. S., & Stompor, R. 2010, ApJS, 187, 212
Carollo, C. M., Bschorr, T. J., Renzini, A., et al. 2013, ApJ, 773, 112
Cavagnolo, K. W., McNamara, B. R., Nulsen, P. E. J., et al. 2010, ApJ, 720, 1066
Collins, C. A., Stott, J. P., Hilton, M., et al. 2009, Nature, 458, 603
Condon, J. 1992, ARA&A, 30, 575
Condon, J., Cotton, W., Greisen, E., et al. 1998, AJ, 115, 1693
Crawford, C. S., Allen, S. W., Ebeling, H., Edge, A. C., & Fabian, A. C. 1999, MNRAS, 306, 857
Cutri, R. M., & et al. 2013, VizieR Online Data Catalog, 2328, 0
da Cunha, E., Charlot, S., & Elbaz, D. 2008, MNRAS, 388, 1595
Daddi, E., Dickinson, M., Morrison, G., et al. 2007, ApJ, 670, 156
Daly, R. A., Sprinkle, T. B., O'Dea, C. P., Kharb, P., & Baum, S. A. 2012, MNRAS, 423, 2498
De Lucia, G., & Blaizot, J. 2007, MNRAS, 375, 2
De Lucia, G., Springel, V., White, S. D. M., Croton, D., & Kauffmann, G. 2006, MNRAS, 366, 499
Donahue, M., Bruch, S., Wang, E., et al. 2010, ApJ, 715, 881
Donahue, M., Connor, T., Fogarty, K., et al. 2015, ApJ, arXiv:arXiv:1504.00598v1

Dressel, L. L. 1981, ApJ, 245, 25
Edwards, L. O. V., Hudson, M. J., Balogh, M. L., & Smith, R. J. 2007, MNRAS, 379, 100
Egami, E., Rex, M., Rawle, T. D., et al. 2010, A&A, 518, L12
Eilek, J. A., & Shore, S. N. 1989, ApJ, 342, 187
Elbaz, D., Daddi, E., Le Borgne, D., et al. 2007, A&A, 468, 33
Fabian, A. C. 1994, ARA&A, 32, 277
—. 2012, ARA&A, 50, 455
Fanaroff, B. L., & Riley, J. M. 1974, MNRAS, 167, 31P
Fogarty, K., Postman, M., Connor, T., Donahue, M., & Moustakas, J. 2015, ApJ, 813, 117
Fraser-McKelvie, A., Brown, M. J. I., & Pimbblet, K. A. 2014, MNRAS, 444, L63
Gaspari, M., Brighenti, F., & Temi, P. 2015, A&A, 579, A62
Gaspari, M., Ruszkowski, M., & Oh, S. P. 2013, MNRAS, 432, 3401
Giacintucci, S., Markevitch, M., Venturi, T., et al. 2014, ApJ, 781, 9
Gunn, J. E., Siegmund, W. a., Mannery, E. J., et al. 2006, AJ, 131, 2332
Helfand, D. J., White, R. L., & Becker, R. H. 2015, ApJ, 801, 26
Hennawi, J. F., Gladders, M. D., Oguri, M., et al. 2008, AJ, 135, 664
Hicks, A. K., Mushotzky, R., & Donahue, M. 2010, ApJ, 719, 1844
Hlavacek-Larrondo, J., Fabian, A. C., Edge, A. C., & Hogan, M. T. 2012, MNRAS, 424, 224
Hlavacek-Larrondo, J., Allen, S. W., Taylor, G. B., et al. 2013, ApJ, 777, 163
Hopkins, P. F., Hernquist, L., Cox, T. J., Keres, D., & Wuyts, S. 2009, ApJ, 691, 1424
Inagaki, T., Lin, Y.-T., Huang, H.-J., Hsieh, B.-C., & Sugiyama, N. 2015, MNRAS, 446, 1107
Jimenez, R., Bernardi, M., Haiman, Z., Panter, B., & Heavens, A. F. 2007, ApJ, 669, 947
Kennicutt, R. C. 1998, ARA&A, 36, 189
Khochfar, S., & Burkert, A. 2003, ApJ, 597, L117
Lara-López, M. A., Cepa, J., Bongiovanni, A., et al. 2010, A&A, 521, L53
Lauer, T. R., Postman, M., Strauss, M. A., Graves, G. J., & Chisari, N. E. 2014, ApJ, 797, 82
Lauer, T. R., Gebhardt, K., Faber, S. M., et al. 2007, ApJ, 664, 226
Ledlow, M. J., & Owen, F. N. 1996, AJ, 112, 9
Lee, N., Sanders, D. B., Casey, C. M., et al. 2015, ApJ, 801, 80
Li, N., & Thakar, A. R. 2008, Computing in Science and Engineering, 10, 18
Li, Y., & Bryan, G. L. 2014, ApJ, 789, 54
Lidman, C., Suherli, J., Muzzin, A., et al. 2012, MNRAS, 427, 550
Lin, Y.-T., Brodwin, M., Gonzalez, A. H., et al. 2013, ApJ, 771, 61
Lin, Y.-T., & Mohr, J. J. 2004, ApJ, 617, 879
Liu, F. S., Mao, S., & Meng, X. M. 2012, MNRAS, 423, 422
Lutz, D. 2010, GT1_dlutz_4: SEDs and energetics of lensed UV-bright high redshift galaxies, Herschel Space Observatory Proposal, id.593
Malhotra, S. 2011, OT2_smalhotr_3: Herschel Extreme Lensing Line Observations (HELLO), Herschel Space Observatory Proposal, id.1765
Martin, D. C., Fanson, J., Schiminovich, D., et al. 2005, ApJ, 619, L1
McDonald, M., Stalder, B., Bayliss, M., et al. 2016, ApJ, 817, 86
McMullin, J. P., Waters, B., Schiebel, D., Young, W., & Golap, K. 2007, in Astronomical Society of the Pacific Conference Series, Vol. 376, Astronomical Data Analysis Software and Systems XVI, ed. R. A. Shaw, F. Hill, & D. J. Bell, 127
McNamara, B. R., & Nulsen, P. E. J. 2007, ARA&A, 45, 117
—. 2012, New Journal of Physics, 14, 055023
Mittal, R., Whelan, J. T., & Combes, F. 2015, MNRAS, 450, 2564
Morrissey, P., Conrow, T., Barlow, T. A., et al. 2007, ApJS, 173, 682
Noeske, K. G., Faber, S. M., Weiner, B. J., et al. 2007, ApJ, 660, L47
O'Connell, R. W. 1999, ARA&A, 37, 603
O'Dea, C. P., Baum, S. A., Privon, G., et al. 2008, ApJ, 681, 1035
O'Dea, K. P., Quillen, A. C., O'Dea, C. P., et al. 2010, ApJ, arXiv:1006.3796
Oguri, M., Bayliss, M. B., Dahle, H. k., et al. 2012, MNRAS, 420, 3213
Petrosian, V. 1976, ApJ, 209, L1
Pilbratt, G. L., Riedinger, J. R., Passvogel, T., et al. 2010, A&A, 518, L1
Pipino, A., Kaviraj, S., Bildfell, C., et al. 2009, MNRAS, 395, 462
Pipino, A., Szabo, T., Pierpaoli, E., MacKenzie, S. M., & Dong, F. 2011, MNRAS, 417, 2817
Pizzolato, F., & Soker, N. 2005, ApJ, 632, 821
Postman, M., Coe, D., Ben, N., et al. 2012, ApJS, 1689, arXiv:1106.3328v3
Saglia, R. P., Sánchez-Blázquez, P., Bender, R., et al. 2010, A&A, 524, A6
Santini, P., Fontana, A., Grazian, A., et al. 2009, A&A, 504, 751
Schlafly, E. F., & Finkbeiner, D. P. 2011, ApJ, 737, 103
Shankar, F., Buchan, S., Rettura, A., et al. 2015, ApJ, 802, 73
Stott, J. P., Collins, C. A., Burke, C., Hamilton-Morris, V., & Smith, G. P. 2011, MNRAS, 414, 445
Sun, M. 2009, ApJ, 704, 1586
Thomas, D., Maraston, C., Bender, R., & Mendes de Oliveira, C. 2005, ApJ, 621, 673
Thompson, A., Clark, B., Wade, C., & Napier, P. 1980, ApJS, 44, 151
Tremblay, G. R., Gladders, M. D., Baum, S. A., et al. 2014, ApJ, 790, L26
Tremblay, G. R., O'Dea, C. P., Baum, S. A., et al. 2015, MNRAS, 451, 3768
Tremblay, G. R., Oonk, J. B. R., Combes, F., et al. 2016, Nature, 534, 218
Treu, T., Ellis, R. S., Liao, T. X., et al. 2005, ApJ, 633, 174
Vaddi, S., O'Dea, C. P., Baum, S. A., et al. 2016, ApJ, 818, 182
van Dokkum, P. G., & Franx, M. 1996, MNRAS, 281, 985
Von Der Linden, A., Best, P. N., Kauffmann, G., & White, S. D. M. 2007, MNRAS, 379, 867
Vulcani, B., Marchesini, D., De Lucia, G., et al. 2016, ApJ, 816, 86
Wang, J., Overzier, R., Kauffmann, G., Von Der Linden, A., & Kong, X. 2010, MNRAS, 401, 433
Whiley, I. M., Aragón-Salamanca, A., De Lucia, G., et al. 2008, MNRAS, 387, 1253
Wright, E. L., Eisenhardt, P. R. M., Mainzer, A., et al. 2010, AJ, 140, 22
Zahid, H. J., Yates, R. M., Kewley, L. J., & Kudritzki, R. P. 2013, ApJ, 763, 92

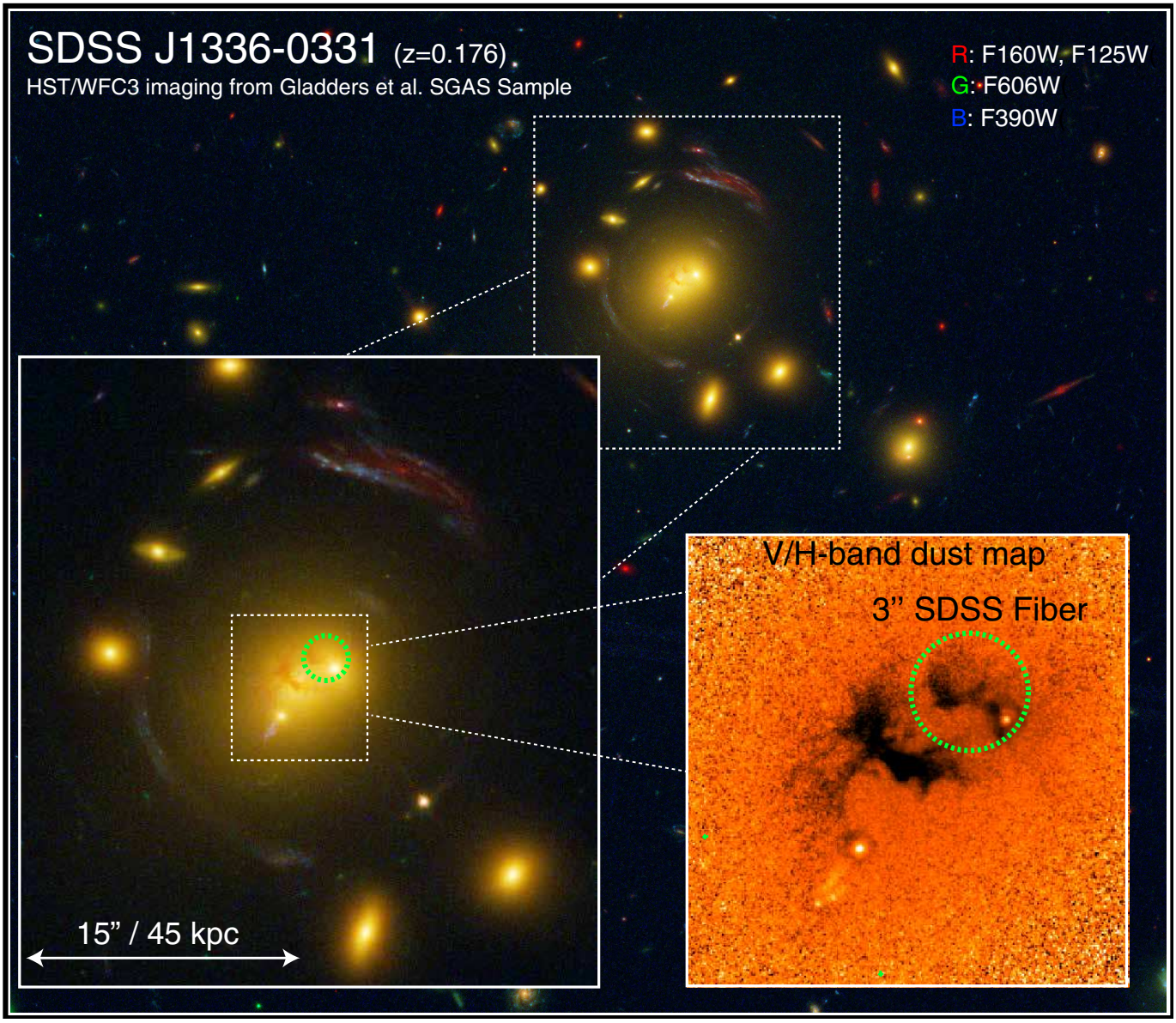

Figure 9. *Left*: HST/WFC3 three color composite observation of cluster SDSSJ1336-0331 (PI: Michael D. Gladders, ID: 13003) with an exposure time of 2400 seconds using filters F390W (blue), F606W (green), and F160W + F125W (red). The green circle indicates the area subtended by the 3" diameter SDSS spectroscopic fiber. Heavy dust obscuration covers the eastern nucleus, and a radial lensed feature is visible near the south-east. The SDSS fiber misses any star formation in much of the south-east. 3" subtends 12.4 kpc at the target redshift. *Bottom Right*: V/H-band color map revealing considerable substructure to the north and east along both nuclei.

Table 1
CLASH & SGAS BCG Samples

Target ID	α_{J2000} (Degrees)	δ_{J2000} (Degrees)	Redshift (z)	Stellar Mass ($M_\odot$)	χ^2	Sample
Abell 209	31:52.6	-13:36:38.80	0.206	4.85e+11	0.599	CLASH
Abell 383	48:03.4	-03:31:44.7	0.187	4.45e+11	5.331	CLASH
Abell 611	00:56.8	+36:03:24.1	0.288	6.58e+11	146.998	CLASH
Abell 1423	57:17.3	+33:36:37.4	0.213	4.83e+11	3.308	CLASH
Abell 2261	22:27.2	+32:07:58.6	0.224	1.23e+12	12.845	CLASH
CLJ1226.9+3332	26:58.4	+33:32:47.4	0.89	1.21e+12	5.748	CLASH
MACS0329.7-0211	29:41.7	-02:11:47.7	0.45	8.47e+11	0.235	CLASH
MACS0416.1-2403	16:09.4	-24:04:03.9	0.42	3.14e+11	0.452	CLASH
MACS0429.6-0253	29:36.1	-02:53:08.0	0.399	1.19e+12	0.004	CLASH
MACS0647.8+7015	47:50.0	+70:14:49.7	0.584	1.47e+12	0.054	CLASH
MACS0710.5+3745	17:31.7	+37:45:18.5	0.548	2.19e+11	0.015	CLASH
MACS0744.9+3927	44:52.8	+39:27:24.4	0.686	7.74e+11	1.175	CLASH
MACS1115.9+0129	15:52.1	+01:29:56.6	0.352	3e+11	2.1	CLASH
MACS1149.6+2223	49:35.9	+22:23:55.0	0.544	4.72e+11	1.907	CLASH
MACS1206.2-0847	06:12.3	-08:48:02.4	0.44	3.13e+11	1.129	CLASH
MACS1211.0-0210	11:01.7	-03:10:39.5	0.494	3.69e+11	1.068	CLASH
MACS1423.8+2404	23:47.8	+24:04:40.5	0.545	5.65e+11	1.145	CLASH
MACS1720.3+3536	20:17.0	+35:36:23.6	0.391	6.59e+11	11.689	CLASH
MACS1931.8-2635	31:49.7	-26:34:34.0	0.352	6.92e+11	12.782	CLASH
MACS2129.4-0741	29:26.1	-07:41:28.8	0.57	9.37e+11	8.04	CLASH
MS2137-2353	40:15.2	-23:39:40.7	0.313	3.65e+11	0.242	CLASH
RXJ1347.5-1145	47:30.6	-11:45:10.1	0.451	4.52e+11	0.026	CLASH
RXJ1532.9+3021	32:53.8	+30:20:58.7	0.345	3.34e+11	12.048	CLASH
RXJ2129.7+0005	29:39.9	+00:05:18.8	0.234	5.81e+11	3.317	CLASH
RXJ2248.7-4431	48:44.3	-44:31:48.4	0.348	8.09e+11	0.065	CLASH
SDSSJ0004-0103	04:51.9	-01:03:15.80	0.479	5.31e+11	0.941	SGAS
SDSSJ0108+0624	08:42.0	+06:24:43.50	0.549	1.67e+11	4.877	SGAS
SDSSJ0146-0929	46:56.0	-09:29:52.40	0.447	9.74e+11	1.036	SGAS
SDSSJ0150+2725	50:00.9	+27:25:36.20	0.3	1.22e+12	171.751	SGAS
SDSSJ0851+3331	51:39.0	+33:31:10.83	0.371	6.5e+11	2.036	SGAS
SDSSJ0915+3826	15:39.0	+38:26:58.77	0.396	...	999.0	SGAS
SDSSJ0928+2031	28:05.6	+20:31:25.55	0.192	...	999.0	SGAS
SDSSJ0952+3434	52:40.0	+34:34:47.09	0.359	4.08e+11	3.055	SGAS
SDSSJ0957+0509	57:39.2	+05:09:31.80	0.447	5.22e+11	0.283	SGAS
SDSSJ1002+2031	02:26.9	+20:31:02.61	0.321	4.91e+11	0.358	SGAS
SDSSJ1038+4849	38:43.2	+48:49:18.73	0.432	2.61e+12	8.098	SGAS
SDSSJ1050+0017	50:39.9	+00:17:06.91	0.3	7.87e+11	3.303	SGAS
SDSSJ1055+5547	55:04.6	+55:48:23.23	0.462	7.59e+11	2.304	SGAS
SDSSJ1110+6459	10:17.6	+64:59:47.02	0.659	3.9e+11	1.592	SGAS
SDSSJ1115+1645	15:04.4	+16:45:38.40	0.191	2.81e+11	2.971	SGAS
SDSSJ1138+2754	38:09.0	+27:54:30.90	0.454	1.91e+11	0.221	SGAS
SDSSJ1152+0930	52:47.3	+09:30:14.54	0.521	8.23e+11	0.537	SGAS
SDSSJ1152+3313	52:00.3	+33:13:41.72	0.357	8.17e+11	2.322	SGAS
SDSSJ1156+1911	56:05.5	+19:11:12.68	0.546	6.14e+11	0.314	SGAS
SDSSJ1207+5254	07:36.4	+52:54:58.20	0.273	7.89e+11	9.278	SGAS
SDSSJ1209+2640	09:23.7	+26:40:46.50	0.559	8.02e+11	2.811	SGAS
SDSSJ1329+2243	29:34.5	+22:43:00.24	0.42	2.57e+12	89.54	SGAS
SDSSJ1336-0331	36:00.0	-03:31:28.63	0.176	6.94e+11	53.666	SGAS
SDSSJ1343+4155	43:32.8	+41:55:04.48	0.418	6.46e+11	41.59	SGAS
SDSSJ1439+1208	39:09.9	+12:08:24.75	0.427	3.24e+11	0.735	SGAS
SDSSJ1456+5702	56:00.8	+57:02:20.60	0.483	8.31e+11	0.672	SGAS
SDSSJ1527+0652	27:45.4	+06:52:31.79	0.394	4.84e+11	0.6	SGAS
SDSSJ1531+3414	31:10.6	+34:14:24.91	0.335	3.05e+11	0.477	SGAS
SDSSJ1604+2244	04:10.2	+22:44:16.69	0.281	3.46e+11	1.368	SGAS
SDSSJ1632+3500	32:10.3	+35:00:30.16	0.475	9.04e+11	0.511	SGAS
SDSSJ1723+3411	23:36.2	+34:11:59.37	0.442	5.39e+11	0.487	SGAS
SDSSJ2111-0114	11:19.4	-01:14:23.57	0.639	3.72e+12	12.035	SGAS

References. — da Cunha et al. (2008), Postman et al. (2012), M.D. Gladders et al. in preparation

Note. — Columns: Target Name, RA(J2000), DEC(J2000), SDSS redshift, MAGPHYS estimated stellar mass ($M_\odot$), fit χ^2 and original subsample. $*$ denotes that RXJ2248.7-4431 is alternately named Abell 1063S.

Table 2
CLASH & SGAS BCG Star Formation Rate Estimators

Target ID	NUV SFR ($M_\odot$/yr)	NUV SFR Error ($M_\odot$/yr)	NUV Quality	Hα SFR ($M_\odot$/yr)	Hα SFR Error ($M_\odot$/yr)	[OII] SFR ($M_\odot$/yr)	[OII] SFR Error ($M_\odot$/yr)
Abell 209	1.85	0.13	D	...	...	...	...
Abell 383	5.74	1.08	D	...	...	...	...
Abell 611	...	...	N	...	...	0.06	0.10
Abell 1423	...	...	N	...	...	...	...
Abell 2261	...	...	N	0.09	0.07	0.01	0.04
CLJ1226.9+3332	1.85	0.402	L	...	...	...	...
MACS0329.7-0211	13.20	0.92	D	...	...	...	...
MACS0416.1-2403	3.11	0.80	L	...	...	...	...
MACS0429.6-0253	...	...	N	...	...	...	...
MACS0647.8+7015	...	...	N	...	...	...	...
MACS0710.5+3745	...	...	N	...	...	...	...
MACS0744.9+3927	...	...	N	0.41	0.12	...	...
MACS1115.9+0129	5.38	0.59	D	2.83	0.19	3.91	0.37
MACS1149.6+2223	4.74	2.04	L	...	...	...	...
MACS1206.2-0847	...	...	N	...	...	...	...
MACS1211.0-0210	...	...	N	...	...	...	...
MACS1423.8+2404	7.6	1.47	D	...	...	...	...
MACS1720.3+3536	...	...	N	...	...	...	...
MACS1931.8-2635	49.51	4.72	D	...	...	...	...
MACS2129.4-0741	4.74	2.32	L	...	...	...	...
MS2137-2353	2.21	0.09	L	...	...	...	...
RXJ1347.5-1145	7.55	0.44	D	...	...	...	...
RXJ1532.9+3021	...	...	N	31.88	0.38	43.53	1.36
RXJ2129.7+0005	1.71	0.64	D	1.71	0.05	2.81	0.19
RXJ2248.7-4431	...	...	N	...	...	...	...
SDSSJ0004-0103	1.33	0.37	L	...	...	...	...
SDSSJ0108+0624	...	...	N	...	...	...	...
SDSSJ0146-0929	...	...	N	0.09	0.03	...	...
SDSSJ0150+2725	2.54	1.04	L	...	...	...	...
SDSSJ0851+3331	0.19	0.42	L	...	...	...	...
SDSSJ0915+3826	1.91	0.55	L	0.28	0.127	0.03	1.02
SDSSJ0928+2031	0.17	0.06	L	0.16	0.08	...	...
SDSSJ0952+3434	1.72	0.67	L	0.55	0.039	...	...
SDSSJ0957+0509	...	...	N	...	...	...	...
SDSSJ1002+2031	...	...	N	0.03	0.04	...	...
SDSSJ1038+4849	7.6	2.04	L	...	...	0.14	0.25
SDSSJ1050+0017	0.7	0.28	L	...	...	...	...
SDSSJ1055+5547	...	...	N	...	...	1.51	1.92
SDSSJ1110+6459	...	...	N	...	...	...	...
SDSSJ1115+1645	0.25	0.18	L	0.04	0.01	0.04	0.17
SDSSJ1138+2754	8.22	2.76	L	...	...	...	...
SDSSJ1152+0930	...	...	N	...	...	0.13	0.42
SDSSJ1152+3313	...	...	N	0.10	0.10	0.14	0.19
SDSSJ1156+1911	3.44	1.37	L	...	...	...	...
SDSSJ1207+5254	0.28	0.13	L	0.20	0.10	0.07	0.07
SDSSJ1209+2640	...	...	N	...	...	0.11	1.50
SDSSJ1329+2243	0.99	0.31	L	...	...	...	...
SDSSJ1336-0331	3.76	1.473	D	...	...	1.83	0.53
SDSSJ1343+4155	...	...	N	...	...	...	...
SDSSJ1439+1208	...	...	N	...	...	0.30	1.35
SDSSJ1456+5702	...	...	N	...	...	0.13	0.29
SDSSJ1527+0652	2.23	1.085	L	...	...	...	...
SDSSJ1531+3414	...	...	N	1.60	0.44	1.94	1.01
SDSSJ1604+2244	...	...	N	...	...	0.07	0.11
SDSSJ1632+3500	0.76	0.43	L	...	...	...	...
SDSSJ1723+3411	...	...	N	...	...	...	...
SDSSJ2111-0114	...	...	N	...	...	...	...

Note. — Columns: Target Name, NUV star formation rate and error, NUV data quality (N - no data, L - 95% Confidence Upper Limit, D - detection), Hα SFR and error, [OII] SFR and error. All star formation rates are in units of $M_\odot$yr and errors represent 1σ values.